Time scales of magma transport and mixing at Kīlauea Volcano, Hawai'i

Auriol S.P. Rae et al.

2016153_Profiles.xlsx

2016153_Summary.xlsx

Methods

Olivine crystals were picked from crushed lapilli erupted during episodes 1, 3, 5, 8, 10, and 15, collected from well-characterised pits during 2008 and 2009 (Sides, 2012). These samples have been previously used for a melt inclusion study (Sides et al., 2014).

An FEI Quanta 650 FEG-ESEM at the University of Leeds was used to acquire backscatter electron images of selected olivine grains at micron to sub-micron resolution. Crystallographic axes of the selected olivine crystals were determined by in-situ Electron Backscatter Diffraction (EBSD). The imaged crystals were chosen as representative of the whole sample in terms of grain morphology and zonation.

The backscatter images were acquired using accelerating voltages of 20kV. Contrast settings were maximised and brightness settings were correspondingly reduced. EBSD was carried out at the same operating conditions and the samples were analysed immediately after backscatter imaging. EBSD patterns were processed using Oxford Instruments software and used to calculate the orientation of the crystallographic axes relative to the backscatter image. To ensure accurate characterisation of the crystallographic orientation, at least two EBSD points were taken on each crystal which were checked for consistency. Mean angles of deviation of the EBSD orientations were not allowed to exceed 1.

SEM images were subsequently analysed (using ImageJ) to produce greyscale intensity profiles perpendicular to the edge of crystals. Greyscale profiles were selected such that a) some glass remained attached to the crystal, and that b) the thinnest zone seen on the image was processed, thus avoiding sectioning effects and selecting zones only affected by diffusion acting parallel to the plane of the section.

Once the greyscale profiles were collected, selected profiles were analysed using a Cameca SX100 EPA at the University of Cambridge to quantify the major element geochemistry of the olivine crystals and adhering matrix glasses. The forsterite content of an olivine is linearly proportional to the brightness of the olivine in an SEM image, thus by measuring lines of probe points perpendicular to the crystal edge, the greyscale profiles could be calibrated to forsterite composition. At least 4 probe points were used per profile (Fig. DR1).

The operating conditions for the electron probe for analysis of olivine and glass compositions are summarised in Tables DR1 and DR2, respectively. Typical analyses are shown in Tables DR3 and DR4. Full data is supplied as a separate Microsoft Excel Workbook.

Micron-resolution profiles (0.1-1.74 µm) could then be made of forsterite composition with distance perpendicular to the crystal edge by correlating the greyscale value of the profile to the measured forsterite content of the crystal from the electron probe data.

Modelling of the ages of the diffusion zones was achieved by comparing the measured compositional profiles with a simulated library of profiles. The library of simulated diffusion profiles obeying composition-dependent diffusion under a 1-D geometry was calculated using finite-difference software (D. J. Morgan, unpublished). The synthetic profile with the minimum misfit to the collected data could then be used to produce a timescale given a calculated diffusion coefficient. All modelled zones have assumed boundary conditions; that the melt at the crystal edge remains at a constant composition, which is reasonable if one considers that the rate of diffusion of Fe-Mg in melt is considerably faster than diffusion in olivine, and that the core of the crystal remains at the initial composition of the crystal. The initial composition of the crystal is assumed to be homogeneous. If these assumptions were inaccurate, it would not be possible to obtain an accurate fit to the data. A selection of compositional profiles and their modelled fits is shown in Figure DR2.

Here, the experimentally determined diffusion coefficient of Dohmen and Chakraborty (2007) was used. The coefficient depends on temperature, oxygen fugacity, crystallographic orientation, pressure, and composition. For diffusion along [001] in olivine (above oxygen fugacities of 10^{-10}Pa):

$$\log\left(D_{Fe-Mg}\right) = -9.21 - \frac{201000 + (P - 10^5) \times 7 \times 10^{-6}}{2.303RT} + \frac{1}{6}\log\left(\frac{fO_2}{10^{-7}}\right) + 3X_{Fe}$$

where D_{Fe-Mg} is the diffusion coefficient (m^2/s), P is the pressure (Pa), R is the gas constant (J/mol/K), T is the temperature (K), fO_2 is the oxygen fugacity (Pa), and X_{Fe} is the mole fraction of the fayalite component (Dohmen and Chakraborty (2007). To obtain diffusion coefficients along [100] and [010], log(6) needs to be subtracted from the equation above to account for diffusion along the c-axis being 6 times faster than along the a- and b- axes.

The rate of diffusion is highly dependent on temperature (Dohmen and Chakraborty, 2007; Morgan et al., 2006). Defining the temperature for each mixing event recorded by the olivine crystals is not straightforward. It is possible to calculate the temperature of the magma from the MgO content of the quenched glass (Helz and Thornber, 1987) however, the olivine cores are not in equilibrium with their carrier liquids, and therefore must be derived from a more magnesium rich parental magma . It is therefore unclear whether the calculated temperature of the melt corresponds to the temperature at which diffusion occurred. Instead, it places a lower bound on the temperature at which diffusion occurred. An upper bound can be placed by considering the temperature of the parental magma of the olivines.

The temperature of melt can be calculated by using the MgO content of the matrix glass using the thermometer of Helz and Thornber (1987).

$$T = 20.1 \, MgO + 1287$$

where T is the temperature (K) and MgO is in weight percent (Helz and Thornber, 1987).

Olivine temperatures are calculated by deriving a relationship between the magnesium content of melt inclusions, accounting for post-entrapment crystallisation, and the forsterite content of the olivine containing the melt inclusion (Fig. DR3). The data used to derive this relationship was taken from Sides et al. (2014), a melt inclusion study using the same olivine crystals as those analysed in this study. The magnesium content of the liquid from which a given olivine crystallised from could then be determined. This magnesium content could then be used to calculate a temperature using the thermometer of Helz and Thornber (1987). This temperature represents an upper bound on the temperature condition.

The glass and olivine temperatures respectively correspond to the minimum and maximum possible temperatures at which diffusion occurred for each crystal (Helz and Thornber, 1987; Table DR1).

We assumed an oxygen fugacity of NNO-1.7 to NNO-0.5 (Gerlach, 1993; Roeder et al., 2003; Table DR1). Here the value of NNO-1.7 from Roeder et al. (2003) was preferred due to its basis on petrological methods rather than direct gas measurement, nonetheless, using the higher oxygen fugacity value of NNO-0.5 (Gerlach, 1993) causes the timescales to shift down by a factor of ~1.6. This uncertainty is relatively small compared to the uncertainty in temperature and the higher oxygen fugacity produces results similar those presented in Figure DR4. Pressure has negligible effect upon the diffusion coefficient but was assumed to be 1kbar (approximately 3 km depth at lithostatic pressure).

In total, 70 crystals/aggregates were imaged in the SEM. Of these, 44 were analysed to produce compositional profiles and finally, from these 44 crystals/aggregrates, we were able to model the diffusional relaxation profile within 24 crystals. The excluded 20 compositional profiles were rejected during quality assurance, primarily due to the effects of zonation due to growth, which results in a violation of the initial conditions of the model and therefore produces spurious timescales. We ensured that we were only selecting compositional zonation as a result of diffusion by only allowing very close fits between the data and model fits. Several of the 24 modelled profiles had more than one compositional zone, therefore a total of 29 diffusional zones were modelled.

Figure 2 used kernel density estimation to produce probability distributions of composition. The algorithm of (Sheather and Jones, 1991) was used to calculate the bandwidth of the kernels, this method of representation was preferred to using histograms because the bin size selected for histograms can significantly affect the apparent distribution (Rudge, 2008).

Table DR1: Operating conditions of electron probe during olivine

		Operating Conditions: 15keV, 20nA	Spot size: 1 micron	
	Standard	**Typical Detection Limits (ppm)**	**Typical Standard Deviation (ppm)**	
Mg	St Johns Olivine	450	0.78	
Al	Corundum	100	0.01	
Si	Diopside	250	0.77	
Ca	Diopside	90	0.01	
Ti	Rutile	150	0.01	
Cr	Chromium	600	0.06	
Mn	Manganese	850	0.08	
Fe	Fayalite	950	0.5	
Ni	Nickel Oxide	520	0.06	
P	Apatite	125	0.01	

Table DR2: Operating conditions of electron probe during glass analysis

		Operating Conditions: 15keV, 6nA	Spot size: 5 microns	
	Standard	**Typical Detection Limits (ppm)**	**Typical Standard Deviation (wt %)**	
Mg	St Johns Olivine	310	0.25	
Al	Corundum	290	0.22	
Si	Diopside	480	0.90	
Ca	Diopside	450	0.30	
Ti	Rutile	180	0.08	
Cr	Chromium	900	0.08	
Mn	Manganese	1100	0.11	
Fe	Fayalite	1400	0.58	
Ni	Nickel Oxide	1000	0.08	
P	Apatite	400	0.05	
Na	Jadeite	500	0.15	
K	Potassium Feldspar	500	0.08	

Table DR3: Typical olivine compositional data (oxide wt%) recorded using Cameca SX100 EPA along 47.424 micron profile corresponding to the profile seen in Figure 1.

Data Point	MgO	Al2O3	SiO2	CaO	TiO2	Cr2O3	MnO	FeO	NiO	P2O5	Total	Distance (µm)
Ep3_2-1 - Core	46.9463	0.0335	40.4796	0.2801	0.017	0.0656	0.116	12.4025	0.3686	0.0266	100.7358	47.424
Ep3_2-2	47.0588	0.0249	40.4556	0.2771	0	0.056	0.1488	12.164	0.4274	0.0085	100.621	35.568
Ep3_2-3	47.0249	0.03	40.5364	0.2725	0.0156	0.0813	0.1461	12.1582	0.3703	0.0165	100.6518	23.712
Ep3_2-4	46.4889	0.048	40.5673	0.2796	0.024	0.091	0.1556	12.2567	0.3891	0.009	100.3092	11.856
Ep3_2-5 – Rim	45.0148	0.0414	40.175	0.2838	0.0453	0.0861	0.123	14.7506	0.296	0.0032	100.8193	0

Table DR4: Typical glass compositional data (oxide wt%) recorded using Cameca SX100 EPA of glass attached to the crystal rim seen in Figure 1.

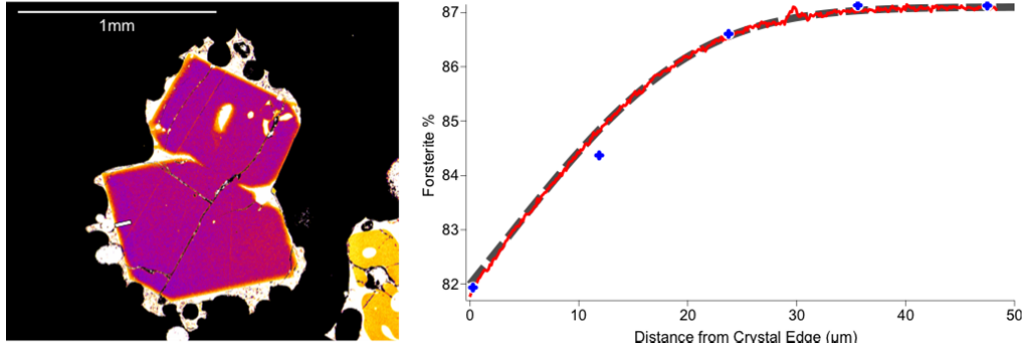| Data Point	MgO	Al2O3	Na2O	SiO2	K2O	Cr2O3	MnO	FeO	TiO2	CaO	P2O5	NiO	Total
Ep3_2-Glass	5.1376	16.6528	2.9116	51.5017	0.5543	0	0.1432	9.4256	2.8358	12.1403	0.3299	0	101.6327

Figure DR1: Calibration and modelling of compositional profiles. Blue points indicate compositions measured by electron probe analysis; the red line shows the calibrated compositional profile, and the grey dashed line shows the modelled fit to the compositional profile. The location of the profile on the crystal is indicated by the white line on the false-coloured backscatter image on the left.
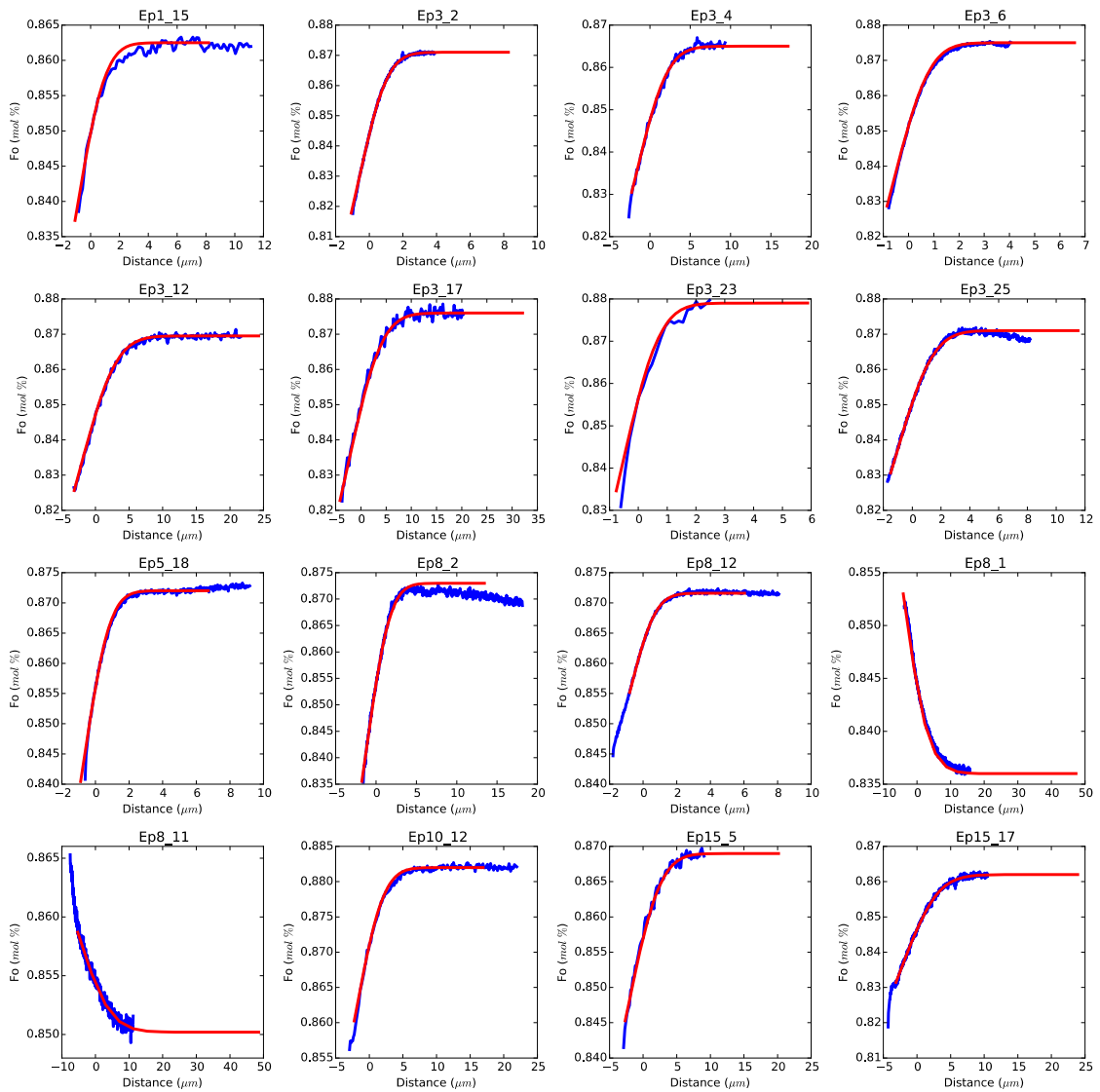

Figure DR2: 16 of the modelled diffusion zones and their fits used in this study. Data derived from SEM images and EPMA calibration are shown with blue lines and their model fits are shown by red lines.
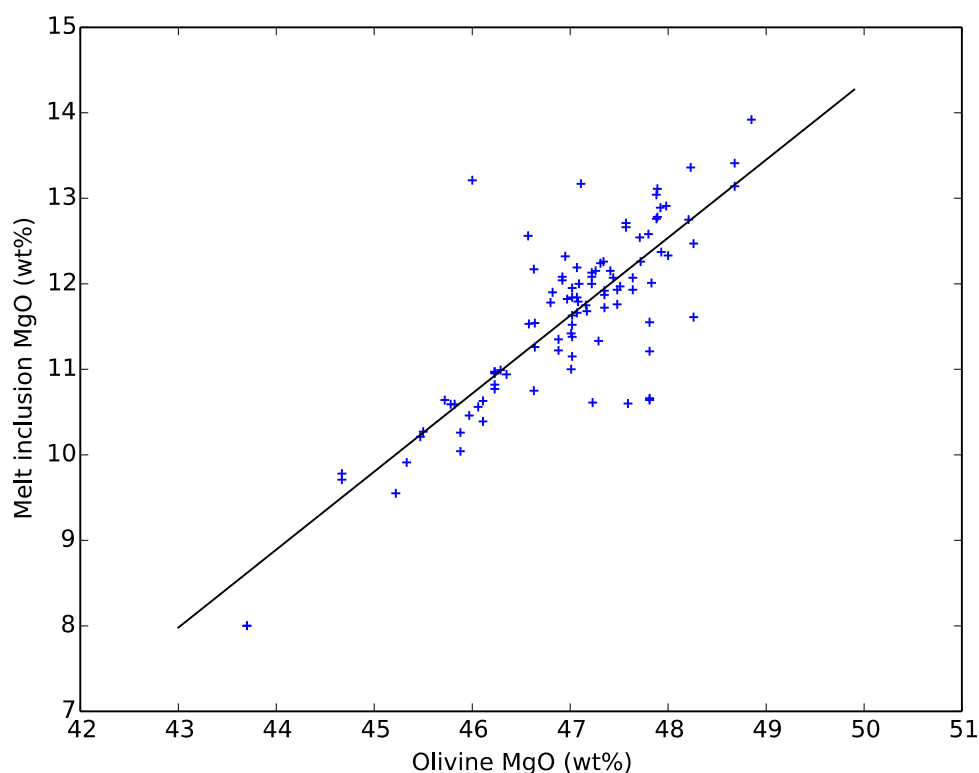
Figure DR3: Olivine magnesium content variation with melt inclusion magnesium content, corrected for post entrapment crystallisation (Sides et al. 2014). The best fit line has the form y=0.9118x – 31.228, with R^2=0.69 where n=99.

REFERENCES

Dohmen, R., Chakraborty, S., 2007. Fe–Mg diffusion in olivine II: point defect chemistry, change of diffusion mechanisms and a model for calculation of diffusion coefficients in natural olivine. Phys. Chem. Miner. 34, 409–430. doi:10.1007/s00269-007-0158-6

Gerlach, T.M., 1993. Oxygen buffering of Kīlauea volcanic gases and the oxygen fugacity of Kīlauea basalt. Geochim. Cosmochim. Acta 57, 795–814. doi:10.1016/0016-7037(93)90169-W

Helz, R.T., Thornber, C.R., 1987. Geothermometry of Kīlauea Iki lava lake, Hawai'i. Bull. Volcanol. 49, 651–668. doi:10.1007/BF01080357

Morgan, D.J., Blake, S., Rogers, N.W., Vivo, B.D., Rolandi, G., Davidson, J.P., 2006. Magma chamber recharge at Vesuvius in the century prior to the eruption of A.D. 79. Geology 34, 845–848. doi:10.1130/G22604.1

Roeder, P.L., Thornber, C., Poustovetov, A., Grant, A., 2003. Morphology and composition of spinel in Pu'u 'O'o lava (1996–1998), Kīlauea volcano, Hawai'i. J. Volcanol. Geotherm. Res. 123, 245–265. doi:10.1016/S0377-0273(02)00508-5

Rudge, J.F., 2008. Finding peaks in geochemical distributions: A re-examination of the helium-continental crust correlation. Earth Planet. Sci. Lett. 274, 179–188. doi:10.1016/j.epsl.2008.07.021

Sheather, S.J., Jones, M.C., 1991. A Reliable Data-Based Bandwidth Selection Method for Kernel Density Estimation. J. R. Stat. Soc. Ser. B Methodol. 53, 683–690.

Sides, I., Edmonds, M., Maclennan, J., Houghton, B.F., Swanson, D.A., Steele-MacInnis, M.J., 2014. Magma mixing and high fountaining during the 1959 Kīlauea Iki eruption, Hawaiʻi. Earth Planet. Sci. Lett. 400, 102–112. doi:10.1016/j.epsl.2014.05.024

Sides, I.R., 2012. Volatile Geochemistry and Eruption Dynamics at Kīlauea Volcano, Hawaiʻi (PhD). University of Cambridge.